Development of finite strain in the convecting lower mantle and its implications for seismic anisotropy

Allen K. McNamara[1] and Peter E. van Keken
Department of Geological Sciences, University of Michigan, Ann Arbor, Michigan, USA

Shun-Ichiro Karato
Department of Geology and Geophysics, Yale University, New Haven, Connecticut, USA

Received 10 May 2002; revised 5 November 2002; accepted 13 December 2002; published 3 May 2003.

[1] Seismological observations have revealed patches of seismic anisotropy in regions related to mantle upwelling and paleosubduction within an otherwise isotropic lower mantle. A combination of numerical modeling and mineral physics is used to constrain the source of anisotropy in these regions in an effort to better understand lower mantle dynamics and mineral physics. Specifically, it is investigated whether lattice-preferred orientation (LPO) can explain the anisotropy observed in regions of paleosubduction. Since LPO is caused by dislocation creep and is destroyed by diffusion creep, we can develop deformation mechanism maps to determine which regions allow for the development of a mineral fabric. Strain is then calculated in these regions and is related to mineral physics experiments combined with high-pressure elastic constants of lower mantle minerals in order to assess the predicted seismic anisotropy. Uncertainties in rheological parameters such as the transition stress between dislocation creep and diffusion creep necessitate a full evaluation of the parameter range. The effect of variations in transition stress, activations parameters, and strength of slabs on fabric development is investigated. It is shown that LPO is a likely candidate for the cause of lowermost mantle anisotropy in regions of paleosubduction. *INDEX TERMS:* 3902 Mineral Physics: Creep and deformation; 7207 Seismology: Core and mantle; 8160 Tectonophysics: Evolution of the Earth: Rheology—general; 8166 Tectonophysics: Evolution of the Earth: Stresses—deep-seated; *KEYWORDS:* mantle convection, anisotropy, dislocation, strain, seismic

Citation: McNamara, A. K., P. E. van Keken, and S.-I. Karato, Development of finite strain in the convecting lower mantle and its implications for seismic anisotropy, *J. Geophys. Res.*, *108*(B5), 2230, doi:10.1029/2002JB001970, 2003.

1. Introduction

[2] Seismic observations reveal patches of seismic anisotropy at the base of an otherwise isotropic mantle [*Lay et al.*, 1998a, 1998b; *Kendall*, 2000]. A better understanding of the cause of this anisotropy may lead to a clearer picture of mantle chemistry and dynamics. Two of the mechanisms for the formation of anisotropy that have been proposed are shape-preferred orientation (SPO) [*Kendall and Silver*, 1996] and lattice-preferred orientation (LPO) [*Karato*, 1998a, 1998b; *Stixrude*, 1998]. It is of considerable interest to determine which of these potential mechanisms lead to the observed anisotropy because SPO requires elastically heterogeneous material, which implies chemical heterogeneity or melting, whereas LPO can occur in a homogeneous material by deformation under high stress. Our approach combines numerical modeling and mineral physics. We show that LPO is the likely cause of anisotropy observed in regions of paleosubduction, removing the need for chemical heterogeneity or partial melting in the lowermost mantle in these regions. We also find that the cause of anisotropy in upwelling regions is not likely caused by LPO due to their low stress state.

1.1. Observations and Causes of Anisotropy

[3] The characteristics of D″ shear wave splitting seem to depend on the tectonic context. Anisotropic patches underneath Alaska [*Garnero and Lay*, 1997], the Caribbean [*Kendall and Silver*, 1996], and the Indian Ocean [*Ritsema*, 2000] are associated with faster than average wave velocities and can be related to locations of paleosubduction [*Lithgow-Bertelloni and Richards*, 1998]. Anisotropy in these regions is consistent with transverse anisotropy with $V_{SH} > V_{SV}$, although azimuthal anisotropy is poorly constrained. The onset of anisotropy occurs 200–250 km above the core-mantle boundary (CMB) and decreases with depth, becoming nearly isotropic directly above the CMB. Shear

[1]Now at Department of Physics, University of Colorado, Boulder, Colorado, USA.

0148-0227/03/2002JB001970$09.00

wave anisotropy in the central Pacific [*Breger and Romanowicz*, 1998; *Ritsema et al.*, 1998; *Russell et al.*, 1998; *Vinnik et al.*, 1998; *Russell et al.*, 1999] is associated with lower than average wave velocities, the presence of ultra-low-velocity zones (ULVZs), and a dense hot spot distribution at the surface. This therefore is likely a region of hot upwelling material. The anisotropy of this region is quite complicated compared to the paleoslab regions, exhibiting subregions of $V_{SV} > V_{SH}$, $V_{SH} > V_{SV}$, or no detectable anisotropy. This anisotropy is observed closer to the CMB than in the paleoslab regions.

[4] Possible causes of D″ anisotropy are discussed by *Karato* [1998a, 1998b], *Lay et al.* [1998a, 1998b], and *Kendall* [2000]. On one hand, SPO can result from oriented melt inclusions or heterogeneous material with a large contrast in elastic constants. LPO, on the other hand, may result from a homogeneous material under high stress that has undergone a significant amount of strain. The development of LPO is linked to the intrinsic elastic anisotropy of mineral components and their deformation mechanisms. The primary components of the lower mantle, (Mg, Fe)SiO_3 and (Mg, Fe)O, have a high degree of intrinsic elastic anisotropy [e.g., *Stixrude*, 1998]. Dislocation creep dominates at high stresses and/or large grain sizes. Strain is accommodated by slip along specific glide planes. An oriented array of anisotropic mineral grains is formed after a significant amount of strain has occurred, resulting in a seismically anisotropic aggregate. Diffusion creep, on the other hand, dominates at low stresses and/or small grain sizes and accommodates strain by the diffusion of atoms or grain boundary sliding. This leads to a random array of anisotropic mineral grains, resulting in a seismically isotropic aggregate. Thus with increasing strain, dislocation creep tends to promote fabric development (LPO), whereas diffusion creep acts to destroy preexisting fabric. It is generally thought that the absence of observed seismic anisotropy in the bulk of the lower mantle is a result of diffusion creep as the dominant deformation mechanism [*Karato et al.*, 1995].

1.2. Results of Previous Work

[5] As a first step toward understanding the cause of lowermost mantle anisotropy, we used numerical modeling of mantle convection to determine the dominant deformation mechanism in an effort to map out regions of the lower mantle in which the development of a fabric is promoted [*McNamara et al.*, 2001]. We observed that in general the deformation of slab regions is dominated by dislocation creep whereas deformation in upwelling regions occurs mostly by diffusion creep. These observations are robust under a wide variation of the controlling rheological parameters. This leads to the conclusion that regions of paleosubduction are suitable for the development of LPO. In contrast, the high degree of diffusion creep at the base of upwellings suggest that other mechanisms, such as SPO, may be required to explain the observed anisotropy.

[6] The domination of dislocation creep indicates that conditions are right for LPO but the extent of fabric development is not revealed. This line of work was extended to determine whether the strain deformation in dislocation creep dominated regions near slabs is consistent with observations of seismic anisotropy near the CMB in regions of paleosubduction [*McNamara et al.*, 2002]. For two different sets of dynamical parameters, we calculated the strain due to dislocation creep in slab regions and compared it to mineral physics experiments [*Yamazaki and Karato*, 2002] to determine the expected seismic anisotropy. For these parameter choices, the strain pattern in slab regions at the base of the mantle is consistent with the $V_{SH} > V_{SV}$ anisotropy observed in regions of paleosubduction. In this paper we will extend this preliminary work and test the sensitivity of our conclusions to a broad range of the governing parameters.

2. Problem Formulation

[7] We perform numerical modeling of mantle convection employing upper and lower mantle rheologies consistent with mineral physics [*Frost and Ashby*, 1982; *Yamazaki and Karato*, 2001], where the creep law incorporates both mechanisms of diffusion and dislocation creep. We examine the geometry of strain that is built up in the dislocation creep dominated regions and compare this to mineral physics experiments that relate seismic anisotropy to strain for (Mg, Fe)O [*Yamazaki and Karato*, 2002].

[8] Uncertainty in rheological parameters necessitates a full evaluation of the parameter range to determine if LPO is the cause of the seismic anisotropy in regions of paleosubduction. We study several effects of varying the rheological parameters, which includes those of weak slabs [*Karato et al.*, 2001], variable transition stresses, different activation parameters, and internal versus bottom heating. We will show that our preliminary results [*McNamara et al.*, 2002] are robust under these varying conditions.

3. Rheology

[9] We employ a composite description of rheology that includes both independent flow mechanisms of diffusion and dislocation creep which is expressed as

$$\dot{\epsilon} = \dot{\epsilon}_{\mathrm{diff}} + \dot{\epsilon}_{\mathrm{disl}}, \tag{1}$$

where $\dot{\epsilon}_{\mathrm{diff}}$ and $\dot{\epsilon}_{\mathrm{disl}}$ are the effective strain rates for diffusion creep and dislocation creep, respectively:

$$\dot{\epsilon}_{\mathrm{diff}} = A'_{\mathrm{diff}} \left(\frac{b}{d}\right)^m \exp\left(-\frac{g_{\mathrm{diff}} T_m}{T_{\mathrm{dim}}}\right) \frac{\sigma}{\mu} \tag{2}$$

$$\dot{\epsilon}_{\mathrm{disl}} = A'_{\mathrm{disl}} \exp\left(-\frac{g_{\mathrm{disl}} T_m}{T_{\mathrm{dim}}}\right) \left(\frac{\sigma}{\mu}\right)^n, \tag{3}$$

where A'_{diff} and A'_{disl} are prefactors, μ and b are reference values for the rigidity and Burgers vector, g_{diff} and g_{disl} are nondimensional empirical parameters that are proportional to activation free energy, T_m is the dimensional melting temperature, T_{dim} is the dimensional temperature, d is the grain size, σ is the stress, and m and n are constants. This formulation is similar to that used by *Karato and Wu* [1993].

[10] Using $\sigma = \eta\dot{\epsilon}$ and rearranging equations (2) and (3) yields an expression for viscosity:

$$\eta = \left(\frac{1}{\eta_{\mathrm{diff}}} + \frac{1}{\eta_{\mathrm{disl}}}\right)^{-1}, \tag{4}$$

where

$$\eta_{\text{diff}} = \frac{\mu}{A'_{\text{diff}}} \left(\frac{d}{b}\right)^m \exp\left(\frac{g_{\text{diff}} T_m}{T_{\text{dim}}}\right) \quad (5)$$

$$\eta_{\text{disl}} = \frac{\mu}{A'_{\text{disl}}} \exp\left(\frac{g_{\text{disl}} T_m}{T_{\text{dim}}}\right) \left(\frac{\sigma}{\mu}\right)^{1-n} \quad (6)$$

where η is the effective viscosity and η_{diff} and η_{disl} are the viscosities for the respective creep mechanisms. This approach is similar to that of *van den Berg et al.* [1993].

[11] There is a transition stress σ_t, at which material flows equally by both mechanisms. Diffusion creep dominates at lower stress whereas dislocation creep dominates at higher stress. The transition stress is calculated by finding the stress at which both creep components have equivalent viscosities:

$$\sigma_t = \left[\left(\frac{A'_{\text{disl}}}{A'_{\text{diff}}}\right)\left(\frac{d}{b}\right)^m \mu^{(1-n)} \exp\left(\frac{T_m}{T}\left(g_{\text{diff}} - g_{\text{disl}}\right)\right)\right]^{\frac{1}{1-n}}. \quad (7)$$

[12] We wish to focus primarily on the properties of the lower mantle, so we use constant parameters that are representative of an olivine rheology ($g_{\text{diff}} = 17$, $g_{\text{disl}} = 31$) for the upper mantle. The activation parameters for dislocation and diffusion creep are different, which lead to a transition stress that increases with decreasing temperature. Mineral physics experiments on MgO, (Mg, Fe)O, and $MgSiO_3$ perovskite suggest that the diffusion creep activation parameter for the lower mantle is between 10 and 14 [*Yamazaki and Karato*, 2001]. The activation parameter for dislocation creep is less constrained, but likely lies between 10 and 18 [*Frost and Ashby*, 1982]. In this study, we maintain $g_{\text{diff}} = 10$ and vary g_{disl} from 10 to 18.

[13] We use the homologous temperature formulation to incorporate the temperature and pressure dependence of viscosity [*Yamazaki and Karato*, 2001]:
Upper mantle

$$T_m = 2100 + 1.4848z - 5 \times 10^{-4} z^2 \quad (8)$$

Lower mantle

$$T_m = 2916 + 1.25z - 1.65 \times 10^{-4} z^2, \quad (9)$$

where temperature is in kelvin and z is the depth in kilometers.

[14] While the activation parameters and melting temperatures are somewhat constrained by mineral physics, there is a large uncertainty in the viscosity prefactors, which lead to uncertainty in the transition stress. The transition stress is only weakly constrained by analogy to experimental work on oxides which limits the ratio of nondimensional prefactors $A'_{\text{disl}}/A'_{\text{diff}}$ between 10^{-8} and 10^{-10} [*Frost and Ashby*, 1982]. Our choice of prefactors is therefore governed by producing a bulk lower mantle that in general is dominated by diffusion creep in order to satisfy seismological constraints [*Karato et al.*, 1995] and by insisting that the resultant viscosity profile is consistent in magnitude and profile with constraints from geoid and postglacial rebound observations [e.g., *Mitrovica and Forte*, 1997]. We will explore a few cases with low transition stresses that lead to a bulk lower mantle dominated by dislocation creep.

[15] The strong temperature dependence of rheology leads to the formation of rigid lid convection. We use a yield stress approach similar to that used by *Tackley* [2000] to break this lid. We limit the maximum stress in the upper 300 km of our models by adjusting the viscosity accordingly. The critical yield stress, σ_c, is a function of depth and includes two components, a constant ductile yield stress, σ_d, and a depth-dependent brittle yield stress that is defined by a brittle stress gradient, σ'_b. The σ_d and σ'_b are related such that they are equal at a depth of 75 km, leading to a near-surface brittle domain and a deeper ductile domain. We found that the correct choice of σ_d to successfully break the lid is quite elusive. In general, it takes many attempts to find an appropriate value. It takes a long model time to determine whether a given value of σ_d would lead to a stable subduction configuration. Often, either a rigid lid will eventually form or the surface plate will degrade into numerous small downwellings. Yet, since we are interested in lower mantle deformation, we can use this approach to generate subducting slabs without requiring a full description of the limitations of this approach. A list of rheological parameters used in this study is included in Table 1.

4. Model Setup

4.1. Convection Equations

[16] The numerical calculations are performed by solving the nondimensional conservation equations of mass, momentum, and energy in the extended Boussinesq approximation [e.g., *Ita and King*, 1994]. The equation for mass conservation in incompressible flow is

$$\nabla \cdot \mathbf{u} = 0 \quad (10)$$

where $\mathbf{u}$ is the velocity vector. The momentum equation is

$$-\nabla P + \nabla \cdot \left(\eta \dot{\underline{\underline{\epsilon}}}\right) = \alpha Ra T \hat{\mathbf{r}}, \quad (11)$$

where $\hat{\mathbf{r}}$ is the radial unit vector, P is the dynamic pressure, η is the effective viscosity (equation (4)), $\dot{\underline{\underline{\epsilon}}}$ is the deviatoric strain rate tensor, α is the nondimensional thermal expansivity, Ra is the Rayleigh number, and T is the temperature. The energy equation includes viscous dissipation and adiabatic (de)compression:

$$\frac{\partial T}{\partial t} + (\mathbf{u} \cdot \nabla) T + \alpha \frac{T_{\text{dim}}}{\Delta T} Diw = \nabla (k \cdot \nabla T) + \frac{Di}{Ra} \sigma_{ij} \frac{\partial u_i}{\partial x_j}, \quad (12)$$

where t is time, k is the nondimensional thermal conductivity, ΔT is the temperature contrast across the model, Di is the dissipation number, w is the radial upward component of velocity, σ_{ij} are components of the stress tensor, and u_i and x_i indicate the ith component of the velocity and location vectors, respectively. The strain rate components are

$$\dot{\epsilon}_{ij} = \frac{\partial u_i}{\partial x_j} + \frac{\partial u_j}{\partial x_i}. \quad (13)$$

The second invariant of the strain rate tensor is the effective strain rate and is represented as

$$\dot{\epsilon} = \left(\frac{1}{2} \Sigma \dot{\epsilon}_{ij} \dot{\epsilon}_{ij}\right)^{\frac{1}{2}}. \quad (14)$$

The Rayleigh number is given as

$$Ra = \frac{\rho_o g \alpha_o \Delta T h^3}{\kappa_o \eta_o}, \quad (15)$$

Table 1. Fixed Parameters[a]

Parameter	Description	Value	Units
ΔT	temperature drop across mantle	3000	K
α_o	reference thermal expansivity	3×10^{-5}	K^{-1}
ρ_o	reference density	4500	kg m^{-3}
C_p	specific heat	1250	J kg^{-1} K^{-1}
h	mantle thickness	2.8×10^6	m
k_o	reference thermal conductivity	5.6	W m^{-1} K^{-1}
g	gravitational constant	9.8	m s^{-2}
κ_o	reference thermal diffusivity	10^{-6}	m^2 s^{-1}
Di	Dissipation number	0.5	
d_{um}	grain size	0.002	m
d_{lm}	grain size	0.001	m
m_{um}	grain-size index	2.5	
m_{lm}	grain-size index	2.5	
n_{um}	power law index	3.0	
n_{lm}	power law index	3.0	
μ	reference rigidity	300	GPa
b	Burgers vector	5.0×10^{-10}	m
$g_{\mathrm{diff-um}}$	olivine diffusion activation parameter	17	
$g_{\mathrm{disl-um}}$	olivine dislocation activation parameter	31	
$g_{\mathrm{diff-lm}}$	lower mantle diffusion activation parameter	10	
R_{surface}	nondimensional surface radius	1.4292	
R_{bottom}	nondimensional bottom radius	0.4292	
$R_{\mathrm{interface}}$	nondimensional upper-lower mantle interface radius	1.19	
η_{max}	nondimensional viscosity maximum	1.0	
η_{min}	nondimensional viscosity minimum	10^{-6}	

[a]Upper and lower mantle values are denoted by um and lm, respectively. The above radii are nondimensionalized by dividing by the length scale, h.

where ρ_o, α_o, κ_o, and η_o are reference values of density, thermal expansivity, thermal diffusivity, and viscosity. The parameter h is the reference length scale corresponding to the depth of the mantle.

[17] The nondimensional viscosity is determined by dividing by the reference viscosity, η_o, which is defined as the diffusion creep viscosity of the olivine layer at $T_{\mathrm{dim}} = 1500$ K and $z = 140$ km. The dissipation number is given as

$$Di = \frac{\alpha g h}{c_p}. \tag{16}$$

[18] We use depth-dependent values of thermal conductivity and thermal expansivity of the nondimensional form

$$\mathrm{k} = \left[\frac{\rho}{\langle\rho\rangle}\right]^3 \tag{17}$$

$$\alpha = \frac{1}{\rho^2}, \tag{18}$$

where the nondimensional density, ρ is given by

$$\rho = \exp\left(\frac{Di}{\gamma} z'\right), \tag{19}$$

where γ is the Grüneisen parameter (set equal to 1) and z' is the nondimensional depth [e.g., *Jarvis and McKenzie*, 1980]. Note that the expression for variable density is only used in the specification of α and k. This parameterization is similar to that used by *Leitch et al.* [1991].

[19] The equations are solved in a two-dimensional (2-D) cylindrical geometry, and the model domain is a quarter cylinder. We employ a radial scaling which maintains the surface area to volume ratio of the model to that of the Earth. This type of scaling has been shown to more adequately represent a spherical Earth in 2-D cylindrical models [*Van Keken*, 2001]. The velocity boundary conditions are free slip.

[20] The equations are solved with the finite element toolbox SEPRAN (http://dutita0.twi.tudelft.nl/sepran/sepran.html). The momentum equation is solved on quadratic triangular elements using a penalty function method [*Cuvelier et al.*, 1986]. The strain rate dependence of viscosity necessitates iterative solution of the momentum and viscosity equations. In most cases a relaxation between successive velocity solutions is required. We do a pointwise iteration to determine stress in the viscosity calculation. A predictor-corrector method with upwinding is used to solve for temperature on linear triangular elements nested within the quadratic elements [*van den Berg et al.*, 1993].

4.2. Strain Equations

[21] The calculation of strain is treated as a postprocessing step along individual tracer particle trajectories. Solution files of temperature and velocity at each nodal point are saved after each Courant time step in the convection calculations. Below, we summarize the calculation of strain; more complete descriptions are given by *Ramsay* [1967], *McKenzie* [1979], and *Spencer* [1980]. The deformation gradient tensor **F** provides a complete description of the finite deformation of a material:

$$\mathbf{F} = \begin{pmatrix} \dfrac{\partial s_x}{\partial x} + 1 & \dfrac{\partial s_x}{\partial y} \\ \dfrac{\partial s_y}{\partial x} & \dfrac{\partial s_y}{\partial y} + 1 \end{pmatrix}. \tag{20}$$

Here s_x and s_y are the x and y components of the displacement in the initial reference frame.

[22] For a given strain marker, the evolution of **F** may be determined by integration with the velocity gradient tensor, **L**:

$$\frac{\partial}{\partial t}F_{ij} = L_{ik}F_{kj}, \tag{21}$$

where

$$\mathbf{L} = \begin{pmatrix} \frac{\partial v_x}{\partial x} & \frac{\partial v_x}{\partial y} \\ \frac{\partial v_y}{\partial x} & \frac{\partial v_y}{\partial y} \end{pmatrix}, \tag{22}$$

where v_x and v_y correspond to the x and y components of velocity, respectively.

[23] Since **F** provides a complete description of deformation it includes rigid rotations. For our purposes it is more convenient to calculate the left Cauchy-Green deformation tensor, **B**, which provides a description of deformation independent of rigid rotations and translations in the deformed coordinates:

$$\mathbf{B} = \mathbf{F} \cdot \mathbf{F}^T. \tag{23}$$

[24] Strain is measured by the stretch which is the ratio of final length to original length. This is provided by the left stretch tensor **V** in the deformed coordinate system. **V** and **B** are related by

$$\mathbf{B} = \mathbf{F} \cdot \mathbf{F}^T = \mathbf{V} \cdot \mathbf{R} \cdot \mathbf{R}^T \cdot \mathbf{V} = \mathbf{V}^2, \tag{24}$$

where **R** is an orthogonal tensor representing rigid rotation. The principal directions and positive square roots of the eigenvalues of $\mathbf{V^2}$ are the directions and magnitudes of maximum and minimum stretch, respectively.

[25] We have tested this approach by comparing numerical results to analytical examples of pure and simple shear as well as more complicated benchmarks [*Ramberg*, 1975]. In addition, we make sure that the conservation of volume has been satisfied for each marker at every time step during the calculation by checking whether the product of maximum and minimum stretches is unity.

[26] We periodically place markers directly above the transition zone in slab regions. The position and strain is calculated by using a fourth-order Runge-Kutta integration scheme. We have found that the Courant time step is sufficiently small enough to ensure accurate strain calculation.

[27] Strain is integrated along the marker path in regions where dislocation creep is the dominant deformation mechanism. Diffusion creep is expected to destroy preexisting fabric due to the randomization of crystal axes. There is a paucity of data on rates of LPO destruction through diffusion creep, so we assume that a preexisting fabric is completely destroyed as material undergoing diffusion creep deforms by twice its original length under diffusion creep. After the marker exits the dislocation creep regime, we continue to calculate the deformation undergone by the material. This allows us to track the direction of the preexisting fabric and the amount of strain that occurs within the diffusion creep regime. We simulate fabric destruction by reducing the stretch as a linear function of further material strain. If a marker reenters the dislocation creep regime before its original strain was destroyed by diffusion creep, the calculation of strain restarts with the current strain ellipsoid as the initial condition.

5. Model Results

[28] We examine strain visually by plotting the maximum stretch minus one, since an undeformed particle has a maximum stretch of unity. A series of convection calculations have been performed that span the relevant parameter range. The calculations are time-dependent, and descriptions of representative snapshots are given below. The list of fixed parameters is given in Table 1, and the list of varied parameters is given in Table 2. A list of global characteristics such as surface heat flow and effective Rayleigh number is given in Table 3.

[29] The first case is entirely bottom heated and incorporates rheological parameters that result in a thick slab that extends to the bottom of the lower mantle without significant buckling. The transition stress is 71 MPa, and the lower mantle activation parameters are equal, which leads to a transition stress that is independent of temperature. The temperature field is shown in Figure 1a. At the surface, the yield stress approach creates a weak region, breaking the lid and allowing the subduction of a cold, high-viscosity slab. The viscosity is shown in Figure 1b. The lower mantle is a couple of orders of magnitude higher in viscosity than the upper mantle (Figure 1c), and the slab itself has 1–2 orders of magnitude higher viscosity than the surrounding lower mantle. Figure 1d shows the ratio of the dislocation creep component of viscosity over the diffusion creep component. Note that when this ratio is positive, diffusion creep dominates the flow, and when this ratio is negative, dislocation creep dominates. The majority of the upper mantle is dominated by dislocation creep except for the inner slab region. This is due to the difference in upper mantle activation parameters which leads to a temperature-dependent transition stress where transition stress increases with decreasing temperature. The bulk of the lower mantle is dominated by diffusion creep, except for the slab and the flanks of the upwellings. Figures 1e–1g show the evolution of strain for markers periodically placed initially above the transition zone. Strain development is rather sluggish for markers in the dislocation creep dominated region of the viscous slab until the slab begins to bend around the CMB. Directly above the CMB a region of laterally directed strain is developed. Note that in this case, as well as those shown below, the highest degree of dislocation-induced strain occurs at the edges of the slabs. While the entire downwelling region produces a high stress regime which imposes dislocation creep domination, a higher degree of deformation (i.e., strain) occurs at the sides of the slab because the viscosity is lower than internal slab regions.

[30] Figure 2 shows results for a convection calculation with different rheological prefactors and a component of internal heating (~30%). The temperature and viscosity maps are shown in Figures 2a and 2b. The viscosity profile is given in Figure 2c. Note that the slab is slightly weaker than the previous case, which leads to a higher degree of buckling as it descends through the lower mantle. The

Table 2. Variable Parameters[a]

Parameter	Figure 1	Figure 2	Figure 3	Figure 4	Figure 4d	Figure 5	Figure 6
A'_{diff} (upper mantle), s^{-1}	2.25×10^{14}	4.51×10^{13}	2.25×10^{13}	4.51×10^{13}	4.51×10^{13}	2.25×10^{13}	4.51×10^{13}
A'_{diff} (lower mantle), s^{-1}	1.06×10^{14}	2.25×10^{14}	1.12×10^{14}	2.25×10^{14}	2.25×10^{14}	1.12×10^{14}	2.25×10^{14}
A'_{disl} (lower mantle), s^{-1}	3.36×10^{5}	7.17×10^{5}	1.79×10^{6}	3.58×10^{5}	7.17×10^{4}	1.79×10^{14}	7.17×10^{5}
g_{disl} (lower mantle)	10	10	10	10	10	18	10
σ_T, MPa	71	71	32	100	224	9	71
σ_d, MPa km^{-1}	400	250	200	250	250	200	250
σ'_b, MPa km^{-1}	5.33	3.33	2.67	3.33	3.33	2.67	3.33
η_o, Pa s	8.7×10^{24}	4.4×10^{25}	8.7×10^{25}	4.4×10^{25}	4.4×10^{25}	8.7×10^{25}	4.4×10^{25}

[a]The σ_T is evaluated at T = 2378 K and depth = 2000 km.

deformation mechanism map is similar to that of the previous case. Again, the bulk of the lower mantle is dominated by diffusion creep except for the slab region. Examination of the strain markers in Figures 2e–2g also show a high degree of lateral strain that is developed directly above the CMB. The progression of strain reveals that there are periods (e.g., Figure 2g) in which the magnitude of developed strain is very low. This illustrates a common feature in all of the convection calculations, a high degree of laterally directed strain directly above the CMB. However, during short time segments this strain pattern may be broken up only to develop once again at a later time.

[31] Given the uncertainties in the parameters that define the transition stress, we have varied its value in the next few cases. The exact numerical values of transition stress given here are not critical. For example, an increase in Rayleigh number is expected to reduce the stress, leading to results more similar to those employing a lower transition stress. It is more important to consider the range of transition stresses from those low enough to produce widespread lower mantle dislocation creep to those high enough to produce dislocation creep only in regions of highest stress. Figure 3 shows results from a case with a lower transition stress (32 MPa). The temperature field is shown in Figure 3a. The deformation mechanism map (Figure 3b) reveals a much greater degree of dislocation creep dominated flow in the lower mantle, which is no longer restricted to the slab region. As expected, the lower transition stress results in a higher degree of fabric development throughout the lower mantle (Figure 3c). Note that the large regions of dislocation creep dominated material lead to a very heterogeneous pattern of strain development throughout the midmantle. As before, however, the slab region directly above the CMB exhibits a high degree of laterally directed strain.

[32] Figure 4 shows results of a model with a higher transition stress (100 MPa). The temperature field and deformation mechanism map are shown in Figures 4a and 4b, respectively. The higher transition stress leads to a much reduced area of dislocation creep domination as compared with the other cases. This in turn, results in reduced fabric development as seen in the strain results of Figure 4c. Although the overall development of strain is reduced, the development of laterally directed strain above the CMB is still present. We perform a calculation with even greater transition stress (224 MPa) and find only very little strain development above the CMB (Figure 4d).

[33] In the cases described thus far, the lower mantle activation parameters were equal which leads to a constant transition stress (equation (7)). Figure 5 shows results in which the dislocation creep activation parameter is increased to 18, which results in a transition stress that decreases with increasing temperature. The temperature field of the snapshot is shown in Figure 5a. The deformation mechanism map illustrated in Figure 5b shows that dislocation creep dominates large areas in the lower mantle. In addition, the hottest lower mantle regions (near CMB and the upwelling regions) are dominated by dislocation creep whereas the cold slab is dominated by diffusion creep. Examination of the strain calculation (Figure 5c) shows little strain development in the diffusion creep dominated region of the slab. Significant strain is developed within the folds of the slab and at the CMB. The strain directly above the CMB is directed laterally, consistent with other results.

[34] We also explore the possibility that slabs are weaker than the standard temperature-dependent rheology would predict based on the kinematics of grain size differentiation as material passes through the transition zone [*Karato et al.*, 2001]. We do this by reducing the maximum viscosity of the lower mantle which leads to a slab viscosity not much greater than the background lower mantle. The temperature field and deformation mechanism map are shown in Figures 6a and 6b, respectively. The strain results (Figure 6c) are consistent with previous observations of a high degree of laterally directed strain directly above the CMB.

6. Discussion

[35] Our results consistently show a pattern of laterally directed strain in slab regions directly above the CMB under a large variation of parameters. This observation appears to

Table 3. Time-Integrated Output of Convection Calculations

Parameter	Figure 1	Figure 2	Figure 3	Figure 4	Figure 4d	Figure 5	Figure 6
Total model time, Myr	889	1045	1307	1411	1490	1124	1124
Surface heat flow, mW m^{-2}	58	85	84	80	79	98	86
Mantle velocity, cm yr^{-1}	0.94	1.18	1.06	1.12	1.09	1.36	1.17
Surface velocity, cm yr^{-1}	0.76	1.74	1.9	1.37	1.55	2.11	1.91
Upper mantle viscosity, Pa s	9.6×10^{20}	1.0×10^{21}	1.8×10^{21}	9.1×10^{20}	9.3×10^{20}	1.0×10^{21}	1.1×10^{21}
Lower mantle viscosity, Pa s	1.4×10^{23}	9.2×10^{22}	1.2×10^{23}	8.9×10^{22}	8.7×10^{22}	1.1×10^{23}	8.9×10^{22}
Effective Rayleigh number	3.1×10^{6}	4.0×10^{6}	2.8×10^{6}	4.3×10^{6}	4.3×10^{6}	3.5×10^{6}	4.1×10^{6}
Internal heat production, %	0	29	30	29	28	28	29

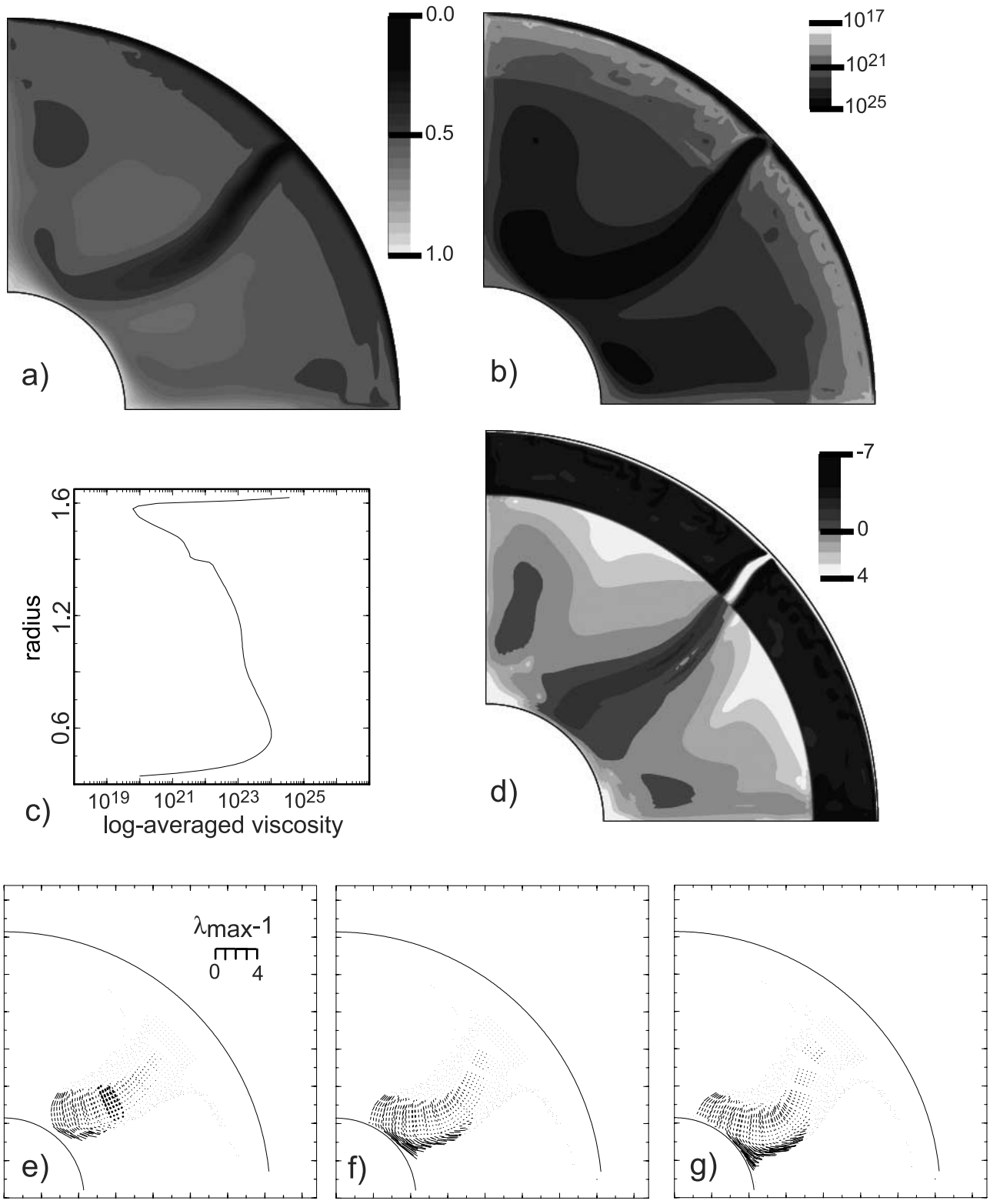

Figure 1. Snapshot of a convection calculation with rheological parameters leading to a thick, stiff slab. The transition stress is 71 MPa. (a) Temperature field in nondimensional units. (b) The logarithm of dimensional viscosity (Pa s). (c) A radial profile of the log averaged viscosity. (d) Deformation mechanism map illustrating the ratio of dislocation creep viscosity to diffusion creep viscosity. Negative values (dark shading) represent dislocation creep dominated flow. (e–g) Time series in 50 Myr increments showing the evolution of strain near the CMB.

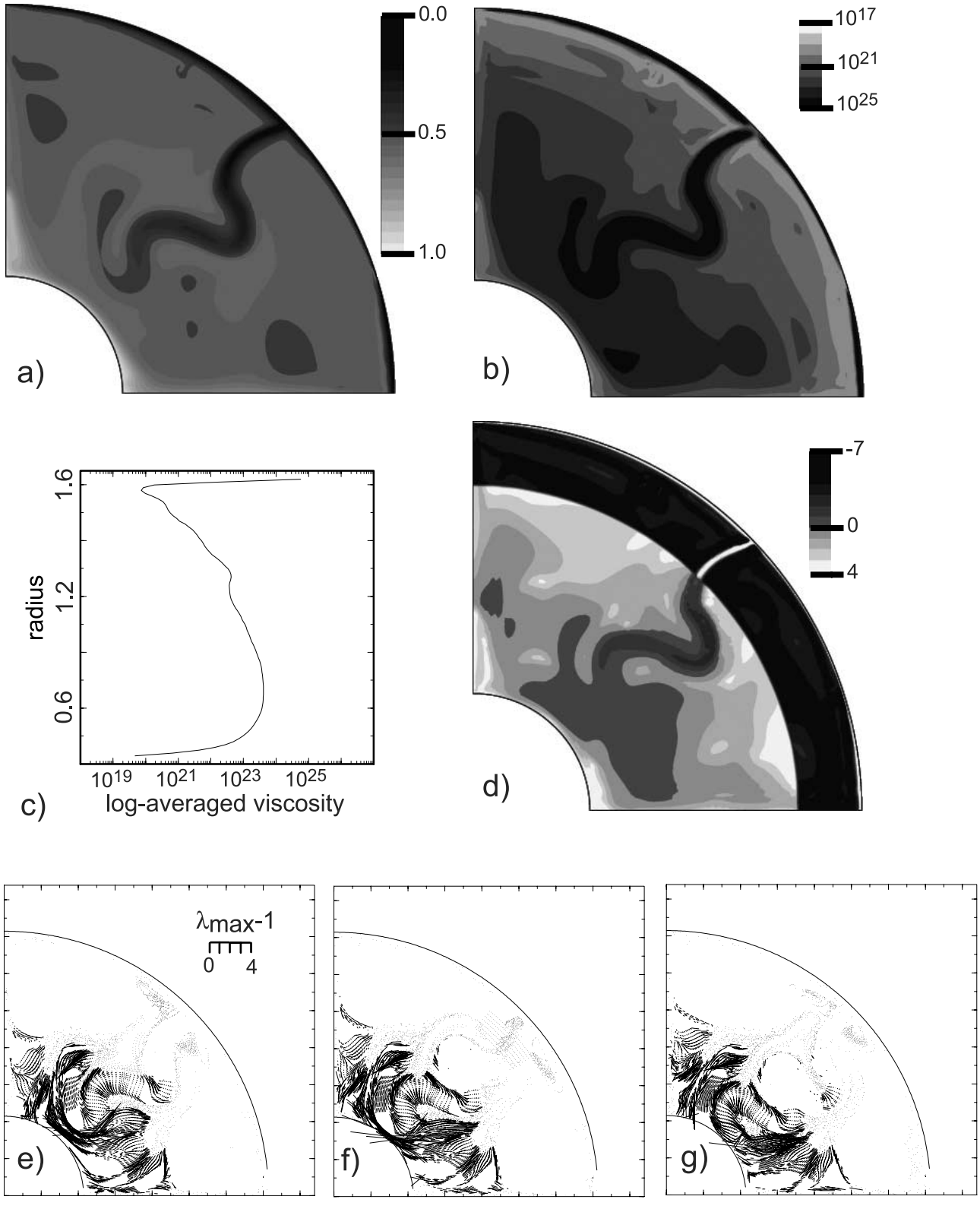

Figure 2. Snapshot of a convection calculation with different rheological parameters. The transition stress is 71 MPa. (a) Temperature field in nondimensional units. (b) Logarithm of dimensional viscosity (Pa s). (c) A radial profile of the log-averaged viscosity. (d) Deformation mechanism map illustrating the ratio of dislocation creep viscosity to diffusion creep viscosity. Negative values (dark shading) represent dislocation creep dominated flow. (e–g) Time series in 50 Myr increments showing the evolution of strain near the CMB.

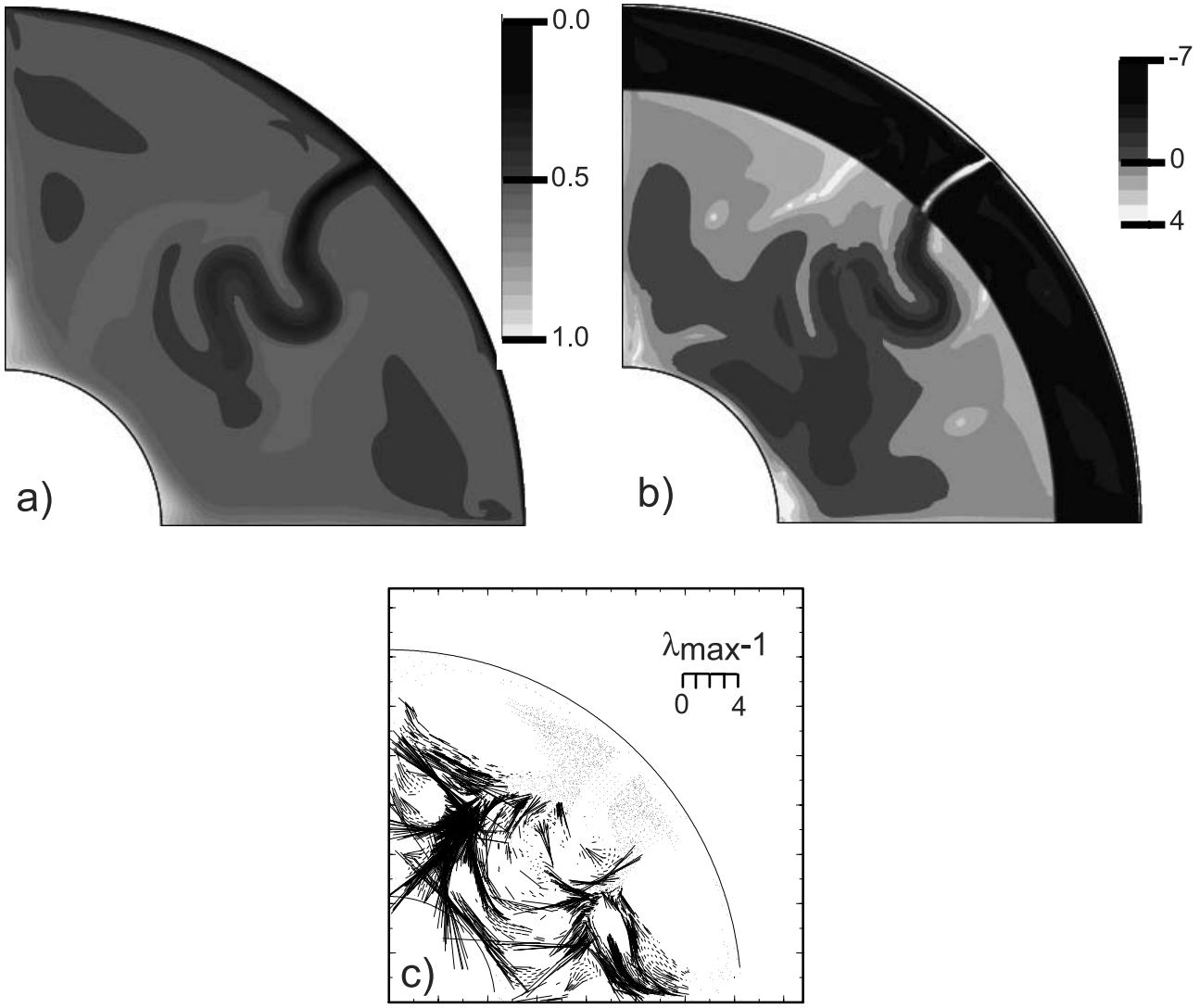

Figure 3. Snapshot of a convection calculation with rheological parameters leading to a lower transition stress of 32 MPa. (a) Temperature field in nondimensional units. (b) Deformation mechanism map illustrating the ratio of dislocation creep viscosity to diffusion creep viscosity. Negative values (dark shading) represent dislocation creep dominated flow. (c) Set of strain markers illustrating how strain evolved throughout the lower mantle.

be independent of heating mode, slab strength, and lower mantle activation parameters. This result appears robust and is linked to the squeezing of slab material as it impinges upon the CMB. As material is forced to change its flow direction, it is stretched laterally. The strongest qualitative control on strain development is the transition stress, which is defined primarily by the rheological prefactors. As the transition stress exceeds 100 MPa, strain development becomes extremely weak. Laterally directed strain occurs directly above the CMB but is likely too small in magnitude to develop a detectable fabric. If the transition stress is too low, a large degree of laterally directed strain is developed above the CMB. However, much greater portions of the mantle exhibit large dislocation creep-induced strain as well. Increasing the activation parameter for lower mantle dislocation creep also extends the degree of dislocation creep in the lower mantle. Although a larger activation parameter tends to cause diffusion creep to dominate in the colder slab portions, a large degree of laterally directed strain is formed directly above the CMB in slab regions.

[36] Mineral physics experiments provide the link between the convection calculations and development of anisotropy. Ideally, one would perform first-principle calculations of mineral aggregates using deformations derived from the convection calculation [e.g., *Wenk and Christie*, 1991; *Blackman et al.*, 1996; *Tommasi et al.*, 2000]. Unfortunately, difficulties associated with the role of dynamic recrystallization and the critical shear stresses associated with specific slip systems make such first-principle calculations unattractive. Here we have chosen an empirical approach by considering strain as a proxy for fabric development. Detailed experimental studies of LPO development have been performed for (Mg, Fe)O [*Yamazaki and Karato*, 2002] and show that LPO is formed as a function of strain in materials deformed by dislocation creep. This study has found that shear strains of ~200% are required to develop significant

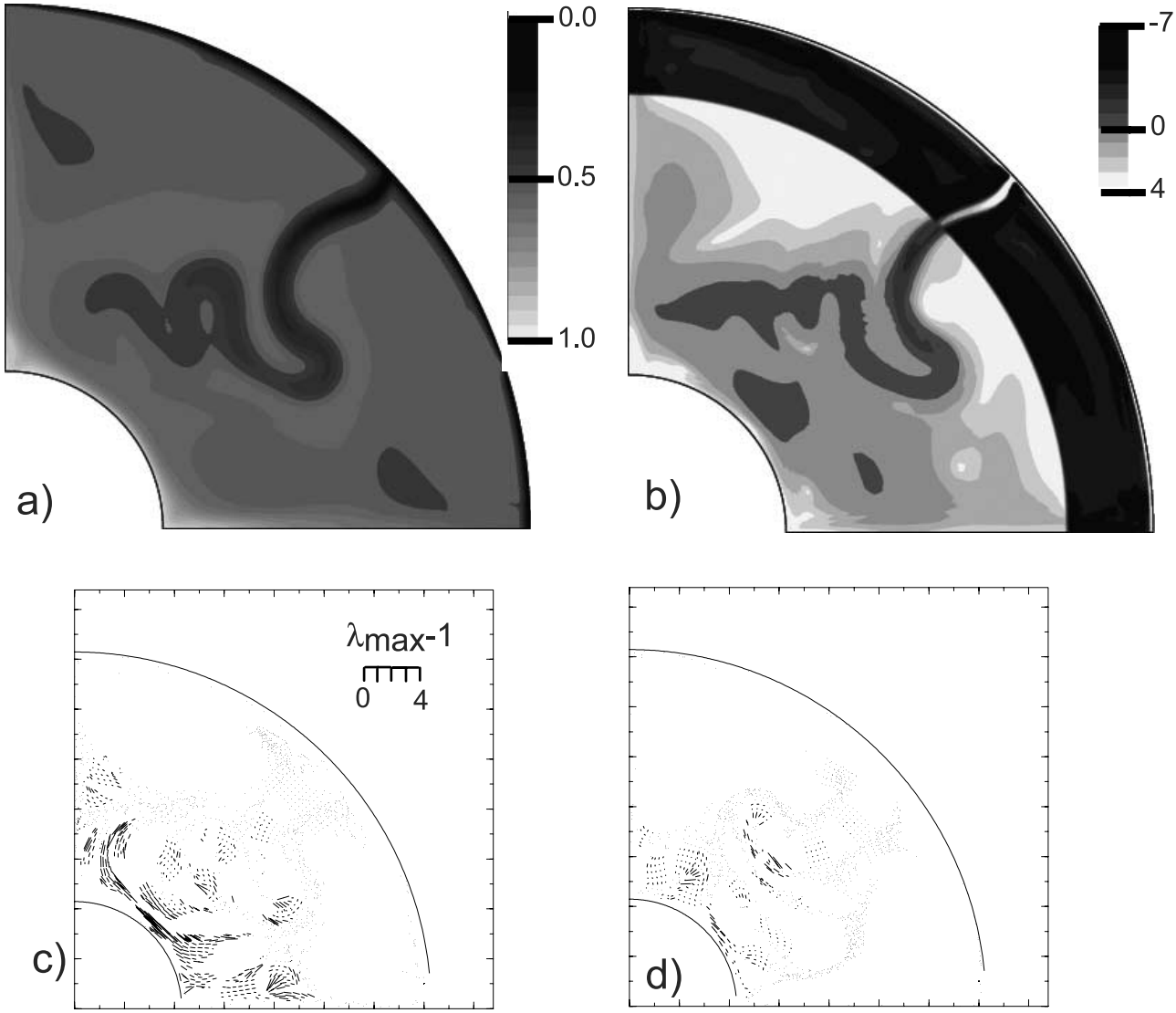

Figure 4. Snapshot of a convection calculation with rheological parameters leading to a higher transition stress of 100 MPa. (a) Temperature field in nondimensional units. (b) Deformation mechanism map illustrating the ratio of dislocation creep viscosity to diffusion creep viscosity. Negative values (dark shading) represent dislocation creep dominated flow. (c) Set of strain markers illustrating how strain evolved throughout the lower mantle. (d) Strain markers from a similar run with a higher transition stress of 224 MPa.

LPO in (Mg, Fe)O and larger strains of 400–500% are sufficient to form steady state LPO. By applying high-pressure elastic constants [*Karki et al.*, 1997] to the fabric experiments [*Yamazaki and Karato*, 2002] it is observed that LPO of (Mg, Fe)O resulting from horizontal shear results in $V_{SH} > V_{SV}$ anisotropy.

[37] By relating the mineral physics experiments, combined with high-pressure elastic constants, to our convection results, we find the large laterally directed strains above the CMB in slab regions correspond to $V_{SH} > V_{SV}$ shear wave anisotropy [*Yamazaki and Karato*, 2002]. This is consistent with the style of anisotropy observed in regions of paleo-subduction. Therefore this work shows that LPO of (Mg, Fe)O is a likely mechanism to produce this anisotropy.

[38] Although the major component of the lower mantle, (Mg, Fe)SiO_3 perovskite, makes up ~80% of the lower mantle by volume, we predict (Mg, Fe)O to play a larger role in anisotropy of the lowermost mantle. Not only does (Mg, Fe)SiO_3 perovskite have a lower intrinsic anisotropy than (Mg, Fe)O [*Stixrude*, 1998], but it is likely that (Mg, Fe)O is the weaker phase [*Yamazaki and Karato*, 2001] and undergoes significantly more strain than (Mg, Fe)SiO_3 perovskite in the two-phase system. Moreover, fabric experiments on perovskite analog materials indicate a lower degree of anisotropy exhibiting $V_{SV} > V_{SH}$ anisotropy for horizontal shear [*Karato*, 1998a; *Yamazaki and Karato*, 2001].

[39] The surface velocities in our models are about a factor of 2 less than those exhibited by real plates. We find it difficult to produce stable subduction configurations with higher velocities. Perhaps increased surface velocities will lead to increased buckling in the slab, but they are not

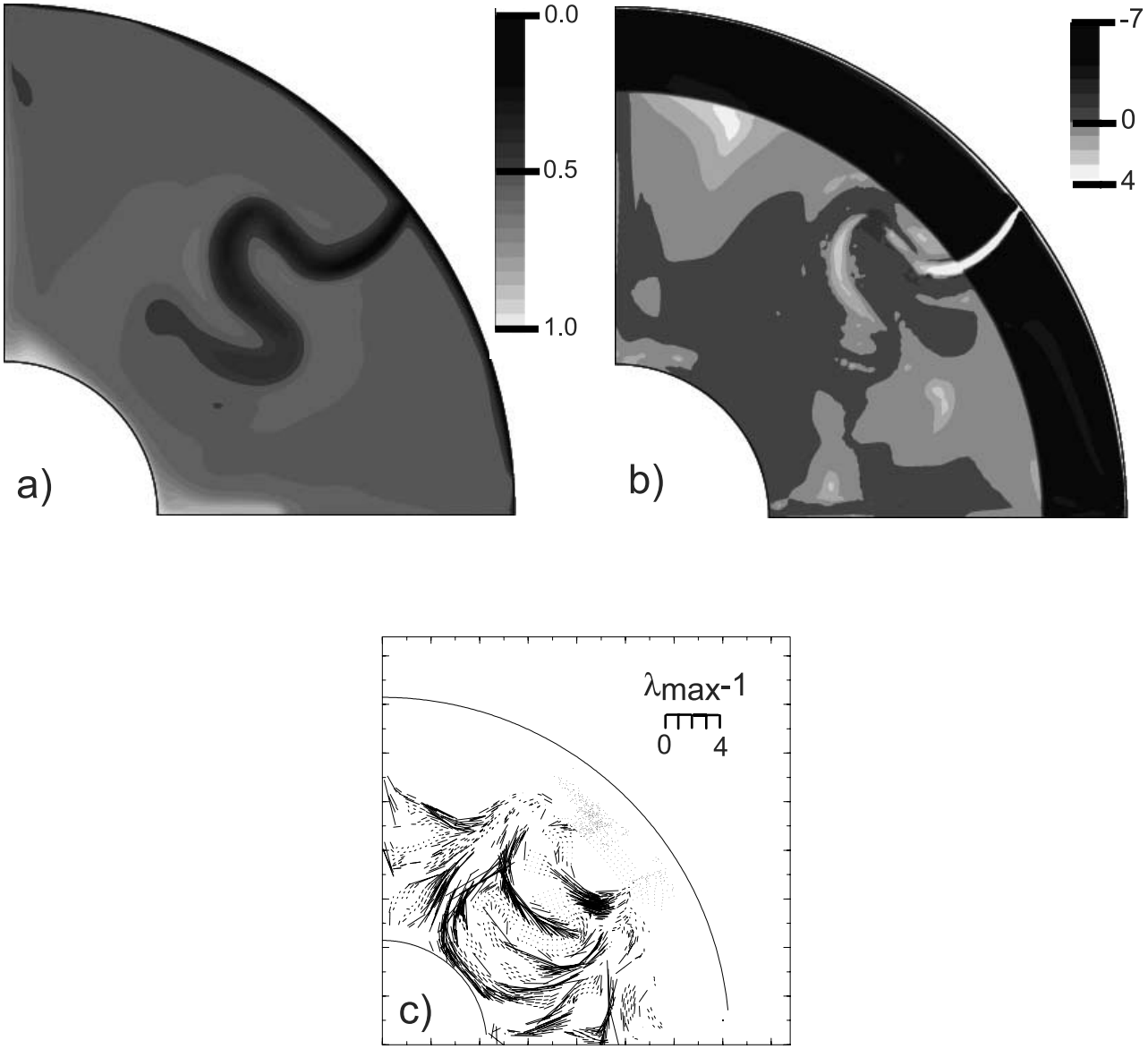

Figure 5. Snapshot of a convection calculation with different lower mantle activation parameters leading to a transition stress that is dependent on pressure and temperature. (a) Temperature field in nondimensional units. (b) Deformation mechanism map illustrating the ratio of dislocation creep viscosity to diffusion creep viscosity. Negative values (dark shading) represent dislocation creep dominated flow. (c) Set of strain markers illustrating how strain evolved throughout the lower mantle.

expected to change the resulting strain pattern. Also, the amount of internal heat generation is only ~30%, which is likely lower than that of the Earth [*Davies*, 1998]. Increasing heat production would decrease the size of upwelling plumes but would not be expected to change the subduction and resultant strain patterns.

[40] A high degree of laterally directed strain is a general feature in our calculations, but during brief periods of time this strain pattern can be broken up and consequently reduced in magnitude. This break up is due to changes in the slab-induced flow pattern. These results would predict that we expect to see seismic anisotropy in most regions of paleosubduction but not necessarily in all regions. Further mapping of the extent of lowermost mantle anisotropy will allow tests of this hypothesis.

[41] The lack of seismic anisotropy throughout the bulk of the lower mantle has intimated the dominance of diffusion creep [*Karato et al.*, 1995]. Results from calculations utilizing a low transition stress or high-dislocation creep activation parameter reveal substantial regions of dislocation creep within the lower mantle (Figures 3 and 5). Although these results could be disregarded because they do not fit the constraint of a diffusion creep dominated bulk lower mantle, another possibility is based on the examination of dislocation creep-induced strain in these cases. The strain pattern formed at the base of subduction regions is consistent with our other calculations, but we find large dislocation creep-induced strains in the midmantle as well. This large midmantle strain fails to form a coherent pattern, and given the reduction in intrinsic anisotropy at lower

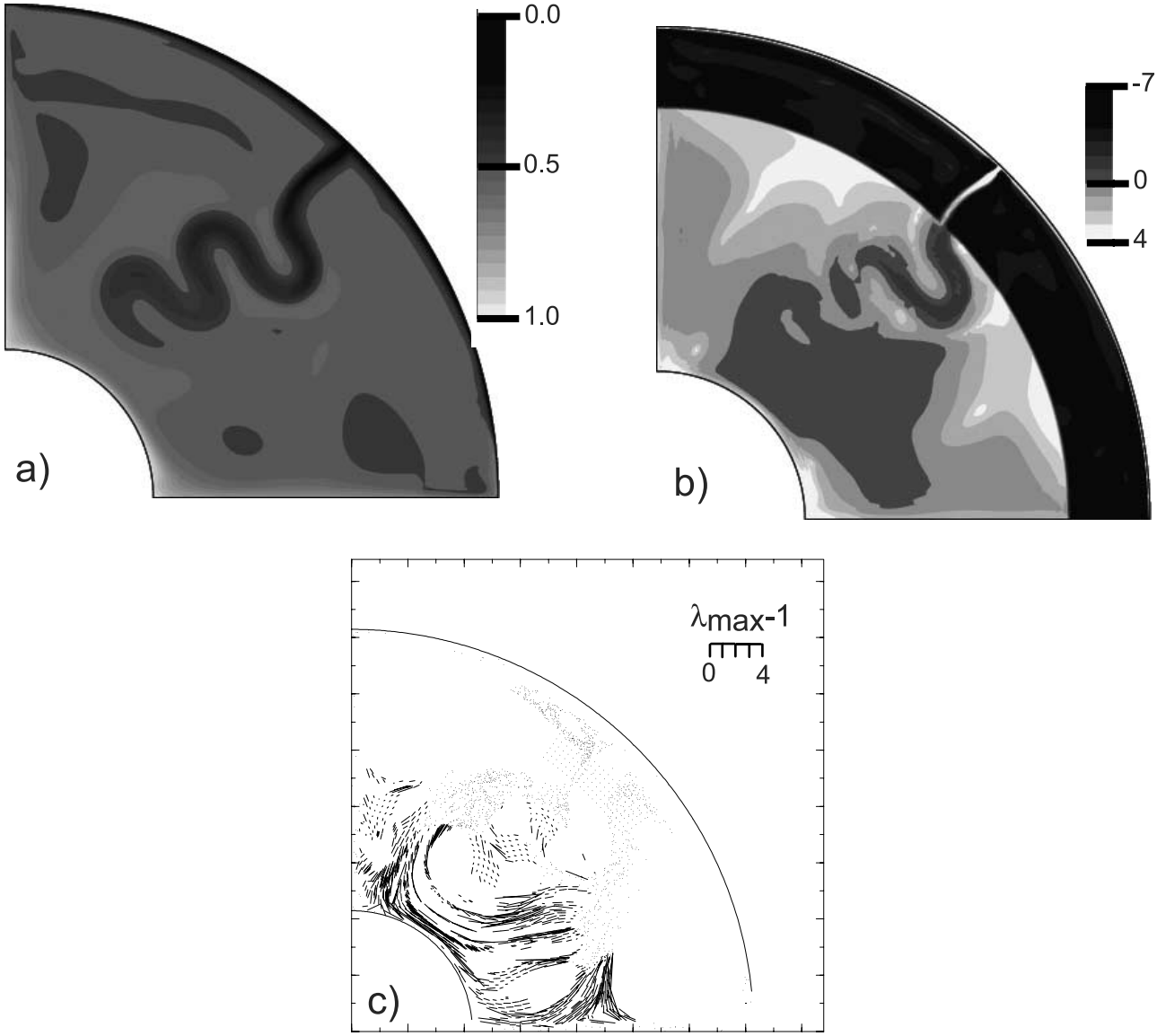

Figure 6. Snapshot of a convection calculation in which the maximum viscosity of the lower mantle is reduced in order to simulate a weak slab. (a) Temperature field in nondimensional units. (b) Deformation mechanism map illustrating the ratio of dislocation creep viscosity to diffusion creep viscosity. Negative values (dark shading) represent dislocation creep dominated flow. (c) Set of strain markers illustrating how strain evolved throughout the lower mantle.

pressures [*Stixrude*, 1998], it may appear isotropic for midmantle ray paths. Further calculations which allow strain markers to mix over much longer times along with seismic ray tracing will be required to test whether this may indeed be the case.

[42] The cause of seismic anisotropy observed at the base up upwelling regions is less clear. Low stresses associated with the reduction in viscosity due to increased temperature indicate that diffusion creep dominates in these regions. Perhaps some type of SPO such as oriented melt inclusions is required to explain the complex anisotropy observed in the central Pacific. Another explanation is based on the hypothesis that slabs induce upwellings at the base of the mantle [*Tan et al.*, 2002]. Because of the sluggish decay of preexisting fabric the laterally oriented strain may turn to vertical in the upwellings. As a preliminary test to such a possibility, we performed strain calculations on a convection calculation in which a slab descended along a side boundary and upwellings originated in the center of the model (see Figure 7a). Figure 7b shows the deformation mechanism map. The slab exhibits flow primarily by dislocation creep whereas the plumes are dominated by diffusion creep. Examination of strain markers (Figure 7c) shows a laterally directed strain at the base of the slab which is fed into the plume region. As the strain markers exit the dislocation creep dominated slab region, the recorded strain begins to decay, but not before it rotates upon reaching the plume. In general, the rotation of fabric produces a complex pattern with significant vertically directed strain. This rotated fabric would tend to preserve anisotropy for a short

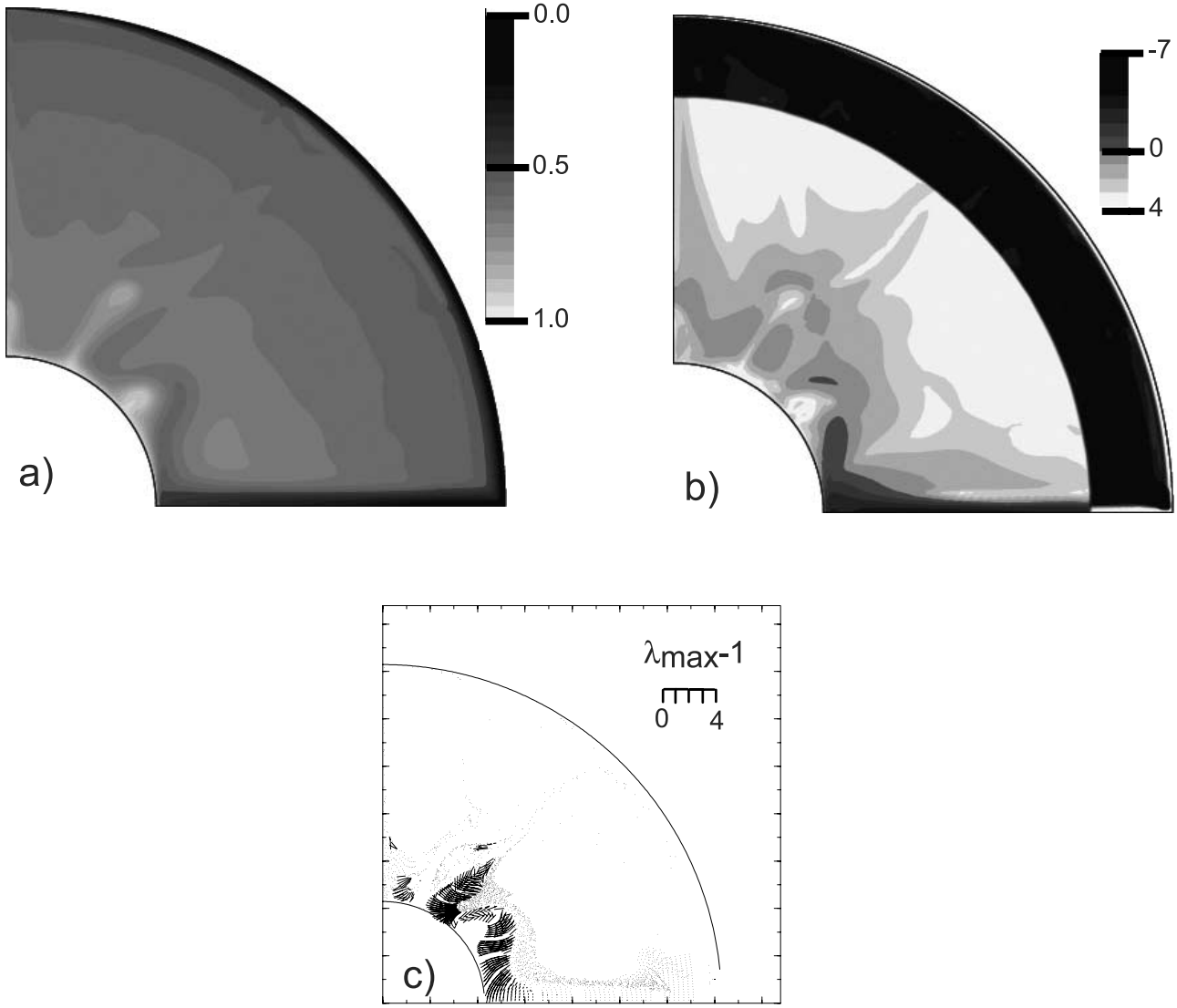

Figure 7. Snapshot of a convection calculation in which slab material feeds an upwelling zone. (a) Temperature field in nondimensional units. (b) Deformation mechanism map illustrating the ratio of dislocation creep viscosity to diffusion creep viscosity. Negative values (dark shading) represent dislocation creep dominated flow. (c) Set of strain markers illustrating how strain evolved throughout the lower mantle.

time, but exhibiting regions of $V_{SV} > V_{SH}$ as well as $V_{SH} > V_{SV}$, not inconsistent with observations.

7. Conclusions

[43] The combination of convection modeling with mineral physics based rheology, strain calculations, LPO experiments, and application of high-pressure elastic constants suggest that $V_{SH} > V_{SV}$ shear wave anisotropy can be expected at the base of the lower mantle in regions of paleosubduction. This result remains robust under a wide range of rheological parameters. The likelihood of LPO as the source of anisotropy in these regions removes the need for chemical heterogeneity [e.g., *Kendall and Silver*, 1996] in slab regions. The source of the more complex anisotropy observed in the central Pacific is less clear, although SPO through melt inclusions remains a likely candidate. An alternative although speculative suggestion is based on the introduction of preexisting fabric from surrounding slab regions.

[44] **Acknowledgments.** We wish to thank D. Yamazaki, T. Lay, M. Gurnis, R. van der Voo, C. Lithgow-Bertelloni, L. Stixrude, and C. Doering for insightful discussions and Scott King and Shijie Zhong for constructive reviews. This research was supported by the National Science Foundation (CSEDI EAR 9905601).

References

Blackman, D. K., J. M. Kendall, P. R. Dawson, H.-R. Wenk, D. Boyce, and P. Morgan, Teleseismic imaging of subaxial flow at mid-ocean ridges: Traveltime effects of anisotropic mineral texture in the mantle, *Geophys. J. Int.*, *127*, 415–426, 1996.

Breger, L., and B. Romanowicz, Three-dimensional structure at the base of the mantle beneath the central Pacific, *Science*, *282*, 718–720, 1998.

Cuvelier, C., A. Segal, and A. A. Steenhoven, *Finite Element Methods and Navier-Stokes Equations*, D. Reidel, Norwell, Mass., 1986.

Davies, G., Topography: A robust constraint on mantle fluxes, *Chem. Geol.*, *145*, 479–489, 1998.

Frost, H. J., and M. F. Ashby, *Deformation Mechanism Maps*, 167 pp., Pergamon, New York, 1982.

Garnero, E. J., and T. Lay, Lateral variations in lower most mantle shear wave anisotropy beneath the North Pacific and Alaska, *J. Geophys. Res.*, *102*, 8121–8135, 1997.

Ita, J., and S. D. King, Sensitivity of convection with an endothermic phase change to the form of governing equations, initial conditions, boundary conditions, and equations of state, *J. Geophys. Res.*, *99*, 15,919–15,938, 1994.

Jarvis, G. T., and D. P. McKenzie, Convection in a compressible fluid with infinite Prandtl number, *J. Fluid Mech.*, *96*, 515–583, 1980.

Karato, S., Some remarks on the origin of seismic anisotropy in the D″ layer, *Earth Planets Space*, *50*, 1019–1028, 1998a.

Karato, S., Seismic anisotropy in the deep mantle, boundary layers and the geometry of mantle convection, *Pure Appl. Geophys.*, *151*, 565–587, 1998b.

Karato, S., and P. Wu, Rheology of the upper mantle: A synthesis, *Science*, *260*, 771–778, 1993.

Karato, S., S. Zhang, and H. Wenk, Superplasticity in the Earth's lower mantle: Evidence from seismic anisotropy and rock physics, *Science*, *270*, 458–461, 1995.

Karato, S., M. R. Riedel, and D. A. Yuen, Rheological structure and deformation of subducted slabs in the mantle transition zone: Implications for mantle circulation and deep earthquakes, *Phys. Earth Planet. Inter.*, *127*, 83–108, 2001.

Karki, B. B., L. Stixrude, S. J. Clark, M. C. Warren, G. J. Ackland, and J. Crain, Structure and elasticity of MgO at high pressure, *Am. Mineral.*, *82*, 51–60, 1997.

Kendall, J. M., Seismic anisotropy in the boundary layers of the mantle, in *Earth's Deep Interior: Mineral Physics and Tomography From the Atomic to the Global Scale*, *Geophys. Monogr. Ser.*, vol. 117, edited by S. Karato et al., pp. 133–159, AGU, Washington D. C., 2000.

Kendall, J. M., and P. G. Silver, Constraints from seismic anisotropy on the nature of the lowermost mantle, *Nature*, *381*, 409–412, 1996.

Lay, T., Q. Williams, and E. J. Garnero, The core-mantle boundary layer and deep earth dynamics, *Nature*, *392*, 461–468, 1998a.

Lay, T., Q. Williams, E. J. Garnero, L. Kellogg, and M. E. Wysession, Seismic wave anisotropy in the D″ region and its implications, in *The Core-Mantle Boundary Region*, *Geodyn. Ser.*, vol. 28, edited by M. Gurnis et al., pp. 299–318, AGU, Washington, D. C., 1998b.

Leitch, A. M., D. A. Yuen, and G. Sewell, Mantle convection with internal heating and pressure-dependent thermal expansivity, *Earth Planet. Sci. Lett.*, *102*, 213–232, 1991.

Lithgow-Bertelloni, C., and M. A. Richards, The dynamics of Cenozoic and Mesozoic plate motions, *Rev. Geophys.*, *36*, 27–28, 1998.

McKenzie, D., Finite deformation during fluid flow, *Geophys. J. R. Astron. Soc.*, *58*, 689–715, 1979.

McNamara, A. K., S. Karato, and P. E. van Keken, Localization of dislocation creep in the lower mantle: Implications for the origin of seismic anisotropy, *Earth Planet. Sci. Lett.*, *191*, 85–99, 2001.

McNamara, A. K., P. E. van Keken, and S. Karato, Development of anisotropic structure by solid-state convection in the Earth's lower mantle, *Nature*, *416*, 310–314, 2002.

Mitrovica, J. X., and A. M. Forte, Radial profile of mantle viscosity: Results from the joint inversion of convection and postglacial rebound observables, *J. Geophys. Res.*, *102*, 2751–2769, 1997.

Ramberg, H., Particle paths, displacement and progressive strain applicable to rocks, *Tectonophysics*, *28*, 1–37, 1975.

Ramsay, J. G., *Folding and Fracturing of Rocks*, McGraw-Hill, New York, 1967.

Ritsema, J., Evidence for shear velocity anisotropy in the lowermost mantle beneath the Indian Ocean, *Geophys. Res. Lett.*, *27*, 1041–1044, 2000.

Ritsema, J., T. Lay, E. J. Garnero, and H. Benz, Seismic anisotropy in the lowermost mantle beneath the Pacific, *Geophys. Res. Lett.*, *25*, 1229–1232, 1998.

Russell, S. A., T. Lay, and E. J. Garnero, Seismic evidence for small-scale dynamics in the lowermost mantle at the root of the Hawaiian hotspot, *Nature*, *396*, 255–258, 1998.

Russell, S., T. Lay, and E. J. Garnero, Small-scale lateral shear velocity and anisotropy heterogeneity near the core-mantle boundary beneath the central Pacific imaged using broadband *ScS* waves, *J. Geophys. Res.*, *104*, 13,183–13,199, 1999.

Spencer, A. J. M., *Continuum Mechanics*, 183 pp., Addison-Wesley-Longman, Reading, Mass., 1980.

Stixrude, L., Elastic constants and anisotropy of $MgSiO_3$ perovskite, periclase, and SiO_2 at high pressure, in *The Core-Mantle Boundary Region*, *Geodyn. Ser.*, vol. 28, M. Gurnis et al., pp. 83–96, AGU, Washington D. C., 1998.

Tackley, P. J., Self-consistent generation of tectonic plates in time-dependent, three-dimensional mantle convection simulations, 2, Strain weakening and asthenosphere, *Geochem. Geophys. Geosyst.*, *1*, 2000GC000043 [14,420 words] 2000.

Tan, E., M. Gurnis, and L. Han, Slabs in the lower mantle and their modulation of plume formation, *Geochem. Geophys. Geosyst.*, *3*(11), 1067, doi:10.1029/2001GC000238, 2002.

Tommasi, A., D. Mainprice, G. Canova, and Y. Chastel, Viscoplastic self-consistent and equilibrium-based modeling of olivine lattice preferred orientations: Implications for the upper mantle seismic anisotropy, *J. Geophys. Res.*, *105*, 7893–7908, 2000.

van den Berg, A. P., P. E. van Keken, and D. A. Yuen, The effects of a composite non-Newtonian and Newtonian rheology on mantle convection, *Geophys. J. Int.*, *115*, 62–78, 1993.

van Keken, P. E., Cylindrical scaling for dynamical cooling models of the Earth, *Phys. Earth Planet. Inter.*, *124*, 119–130, 2001.

Vinnik, L., L. Breger, and B. Romanowicz, Anisotropic structures at the base of the Earth's mantle, *Nature*, *393*, 564–567, 1998.

Wenk, H. R., and J. M. Christie, Comments on the interpretation of deformation textures in rocks, *J. Struct. Geol.*, *13*, 1091–1110, 1991.

Yamazaki, D., and S. Karato, Some mineral physics constraints on the rheology and geothermal structure of Earth's lower mantle, *Am. Mineral.*, *86*, 385–391, 2001.

Yamazaki, D., and S. Karato, Fabric development in (Mg, Fe)O during large strain, shear deformation: Implications for seismic anisotropy in Earth's lower mantle, *Phys. Earth Planet. Inter.*, *131*, 251–267, 2002.

S.-I. Karato, Department of Geology and Geophysics, Yale University, New Haven, CT 06520-8109, USA.

A. K. McNamara, Department of Physics, University of Colorado, 390 UCB, Boulder, CO 80309-0390, USA. (mcnamar@colorado.edu)

P. E. van Keken, Department of Geological Sciences, University of Michigan, Ann Arbor, MI 48109-1063, USA.